Bioorganic Chemistry 90 (2019) 103085

Contents lists available at ScienceDirect

Bioorganic Chemistry

journal homepage: www.elsevier.com/locate/bioorg

DNA interaction and photodynamic antitumor activity of transition metal mono-hydroxyl corrole

Yan-Mei Sun[a], Waseem Akram[a], Fan Cheng[a], Ze-Yu Liu[a], Yu-Hui Liao[b,*], Yong Ye[a], Hai-Yang Liu[a,*]

[a] School of Chemistry and Chemical Engineering, Key Laboratory of Functional Molecular Engineering of Guangdong Province, South China University of Technology, Guangzhou 510641, China
[b] Molecular Diagnosis and Treatment Center for Infectious Diseases, Dermatology Hospital, Southern Medical University, Guangzhou 510091, China

ARTICLE INFO

Keywords:
Corrole
Transition metal complex
Photodynamic therapy
DNA-binding
Apoptosis

ABSTRACT

A series of iron(III), manganese(III) and copper(III) mono-hydroxyl corrole complexes had been prepared and well characterized by UV–vis, ^{1}H NMR, ^{19}F NMR and HR-MS. These metallocorroles may bind to CT-DNA through external binding mode. Metallocorrole **Fe-2c** exhibited significant phototoxicity and low toxicity toward A549 tumor cells. While manganese (III) and copper (III) corroles showed hypotoxicity to A549, MCF-7 and HepG-2 tumor cells, whether under dark or illumination conditions. All tested metallocorroles exhibited non-toxicity to human normal cells (GES-1) with or without irradiation at 625 nm. Cell cycle analysis indicated that metallocorrole **Fe-2c** arrested the cell cycle at G2/M phase and increased the Sub-G1 phase in A549 cell lines. It was mainly localized at mitochondria and could significantly reduce mitochondrial membrane potential after photodynamic treatment, which would further induce tumor cell apoptosis.

1. Introduction

Photodynamic therapy (PDT) is a noninvasive therapeutic modality for the treatment of a variety of cancerous tumors and non-cancerous diseases, such as lung cancer [1], prostate cancer [2], age-related macular degeneration [3] and infection diseases [4]. This emerging technique requires a non-toxic photosensitizer (PS) which can generate reactive oxygen species (ROS) under harmless light source in the presence of molecular oxygen. The photochemical processes associated with cell death have been classically described by three types of photosensitized reaction. Namely, type-I mechanism, in which the triplet excited state photosensitizer reacts with nearby biological substrates via non-specific electron or proton transfer to form radical, then the generated radical reacts with molecular oxygen to produce ROS such as superoxide (O_2^-). Type-II mechanism involves direct energy transfer from the triplet excited state photosensitizer to surrounding ground state molecular oxygen to generate singlet oxygen($^1O_2$). A less common type-III mechanism happens under hypoxic conditions, in which the excited photosensitizer oxidizes target biomolecules such as DNA directly [5]. As compared to surgery or radiation therapy, PDT has significant advantages in virtue of negligible systemic toxicities and minimal toxicity to normal tissue. Moreover, it may greatly reduce long-term morbidity due to the lack of intrinsic or acquired resistance mechanisms [6]. The PS plays a crucial role in determining the efficiency of PDT. Porphyrin derivative is a kind of the most studied photosensitizer [7,8]. The first clinical photosensitizer used in photodynamic therapy was hematoporphyrin derivative (HpD)-Photofrin, which exhibits high efficiency for the treatment of lung cancer, breast cancer and the skin cancer [9].

Corrole is a tetrapyrrolic macrocycle closely related to porphyrin with one less *meso*-carbon atom and an additional NH proton at inner core. Study on corroles have received much attention in recent years, particularly, their applications in PDT [10,11], catalysis [12], and sensors [13]. Corrole exhibits unusual ability to stabilize high-valent metals such as iron(IV) [14] and manganese(V) [15]. High oxidation metal ions in the core of corrole may cause oxidative damage to nucleobase, leading to strand scission and lipid peroxidation [16,17]. As early as in 2000, 5,10,15-tris(4- (2-pyridyl)-tetrafluorophenyl) corrole was firstly tested on the cell culture of lung carcinoma cells [18]. In 2006, we found mono-hydroxyl corrole exhibited significant photocytotoxicity toward NPC tumor cell lines [19]. It was found that sulfonated gallium(III) corrole could be delivered to target tumor tissue using special carrier proteins [20], and exhibited photodynamic therapy activity [16]. Furthermore, carboxylated gallium(III) corroles

* Corresponding authors.
E-mail addresses: liaoyh8@mail.sysu.edu.cn (Y.-H. Liao), chhyliu@scut.edu.cn (H.-Y. Liu).

https://doi.org/10.1016/j.bioorg.2019.103085
Received 4 February 2019; Received in revised form 22 June 2019; Accepted 24 June 2019
Available online 27 June 2019

were also found to exhibit significant cytotoxicity to cancer cell lines [21]. In recent years, our group have reported the photodynamic antitumor activity of gallium(III) mono-formylphenyl [22], gallium(III) [23] and phosphorus(V) tris(ethoxycarbonyl) corrole [24]. PDT treatment by gallium(III) and phosphorus(V) tris(ethoxycarbonyl) corrole can significantly suppress the growth of cancer xenograft in nude mice without obvious toxic side effect.

The coordinated transition metal may exert significant effect on the PDT of corrole. However, reports on PDT of transition metal corroles are very less. Although manganese(III) pyridylcorrole was found to exhibit high cytotoxic against the ovarian cancer cell line and can induce DNA replication arrest [16]. In porphyrin cases, it has been found copper(II) may enhance the anti-tumor activity of tris(4-acetoxy-3-methoxyphenyl)porphyrin at sub-micromolar concentration level [25]. Also, iron may affect the PDT efficiency of tetra(*p*-benzoato)porphyrin through Fenton-like reaction [26].

Previous studies showed the interaction between anticancer drugs and DNA can induce DNA damage, inhibiting tumor cell growth, and resulting in cell death [27,28]. To explore the PDT activity of transition metal corrole, we herein have prepared Fe (III), Mn (III) and Cu (III) mono-hydroxyl corrole complexes (Scheme 1), their PDT activity towards tumor cells and interactions with DNA had been investigated. Experimental results revealed that iron *para*-mono-hydroxyl corroles exhibited the best photodynamic activity among all these tested transition metal corroles.

2. Experimental

2.1. General

All reagents were purchased from commercial sources and used without further purification unless otherwise mentioned. UV–vis absorption spectra were measured on a Hitachi 3900H spectrophotometer in 1 cm optical path length quartz cells at room temperature. Fluoresce emission spectra were measured using a Hitachi F-4500 fluorescence spectrophotometer. ^{1}H and ^{19}F NMR spectra were recorded on a Bruker Avance III HD 400 MHz spectrometer in $CDCl_3$ solution. HR-MS spectra were recorded on a Bruker maXis impact mass spectrometer with an ESI source. The cancer cells were imaged by Olympus IX71 fluorescence microscopy. Flow cytometric analysis were performed using BD FACSVerse flow cytometer.

All biological experiments were prepared using Ultrapure MilliQ water. A red LED lamp (625 nm) was used as the light source. Cell lines were purchased from the American Type Culture Collection. Cancer cells were cultured in RPMI 1640 or DMEM (GIBCO), with the supplement of 10% fetal bovine serum (FBS; Gibco, US).

2.2. Chemistry

2.2.1. Synthesis of freebase corroles

10-(2-hydroxylphenyl)-5,15-bis(pentafluorophenyl)corrole (**1a**), 10-(3-hydroxylphenyl)-5,15-bis(pentafluorophenyl)corrole (**1b**) and 10-(4-hydroxylphenyl)-5,15-bis(pentafluorophenyl)corrole (**1c**) were synthesized according to the procedures described in the literature [19].

*10-(2-hydroxylphenyl)-5,15-bis(pentafluorophenyl)corrole (**1a**)*. ^{1}H NMR (400 MHz, $CDCl_3$) δ 9.13 (d, J = 4.3 Hz, 2H), 8.73 (d, J = 4.7 Hz, 2H), 8.69 (d, J = 4.7 Hz, 2H), 8.58 (d, J = 4.2 Hz, 2H), 7.92 (d, J = 6.3 Hz, 1H), 7.70 (t, J = 7.9 Hz, 1H), 7.34 (dd, J = 12.4, 7.8 Hz, 2H). ^{19}F NMR (376 MHz, $CDCl_3$) δ −137.60 to −138.18 (m, 4F), −152.49 (t, J = 20.9 Hz, 2F), −161.41 to −161.83 (m, 4F).

*10-(3-hydroxylphenyl)-5,15-bis(pentafluorophenyl)corrole (**1b**)*. ^{1}H NMR (400 MHz, $CDCl_3$) δ 9.13 (d, J = 4.2 Hz, 2H), 8.69 (d, J = 4.8 Hz, 4H), 8.59 (d, J = 4.2 Hz, 2H), 7.70 (d, J = 7.4 Hz, 1H), 7.52 (t, J = 7.8 Hz, 1H), 7.35 (s, 1H), 6.99–6.93 (m, 1H). ^{19}F NMR (376 MHz, $CDCl_3$) δ −137.18 to −138.30 (m, 4F), −152.80 (t, J = 20.9 Hz, 2F), −161.53 to −162.16 (m, 4F).

*10-(4-hydroxylphenyl)-5,15-bis(pentafluorophenyl)corrole (**1c**)*. ^{1}H NMR (400 MHz, $CDCl_3$) δ 9.11 (d, J = 4.3 Hz, 2H), 8.71 (q, J = 4.7 Hz, 4H), 8.57 (d, J = 4.2 Hz, 2H), 8.03 (d, J = 8.2 Hz, 2H), 7.20 (d, J = 8.3 Hz, 2H). ^{19}F NMR (376 MHz, $CDCl_3$) δ −137.88 (dt, J = 20.2, 10.2 Hz, 4F), −152.90 (t, J = 21.0 Hz, 2F), −161.80 (dt, J = 23.7, 7.9 Hz, 4F).

2.2.2. Synthesis of iron (III) corroles

*10-(2-hydroxylphenyl)-5,15-bis(pentafluorophenyl)corrole iron (III) (**Fe-2a**)*. A solution of 10-(2-*h*ydroxylphenyl)-5,15-bis(pentafluorophenyl)corrole (29.7 mg, 0.04 mmol) and iron chloride tetrahydrate (1.2289 g, 6 mmol) in *N*, *N*-dimethylformamide (DMF, 10 mL) was refluxed for 4 h. The reaction mixture was allowed to cool down to room temperature, then CH_2Cl_2 (30 mL) and H_2O (30 mL) were added to the reaction mixture, followed by stirring energetically for 5 min. The organic phase was collected and washed six times with deionized water, dried over Na_2SO_4, filtered and evaporated under reduced pressure to afford crude product. The resulting crude product was purified by chromatography on silica gel with CH_2Cl_2/CH_3OH (100:5) as eluent. The pure product was obtained after recrystallization from CH_2Cl_2/hexane. Yield: 72.90%. HRMS-ESI: *m/z*: calcd. for $C_{37}H_{12}F_{10}FeN_4O$: 775.0274, found: 775.0276.

*10-(3-hydroxylphenyl)-5,15-bis(pentafluorophenyl)corrole iron (III) (**Fe-2b**)*. The synthetic method was similar to **Fe-2a**. Yield: 83.01%. HRMS-ESI: *m/z*: calcd. for $C_{37}H_{12}F_{10}FeN_4O$: 775.0274, found: 775.0279.

*10-(4-hydroxylphenyl)-5,15-bis(pentafluorophenyl)corrole iron (III) (**Fe-2c**)*. The synthetic method was similar to **Fe-2a**. Yield: 80.18%. HRMS-ESI: *m/z*: calcd. for $C_{37}H_{12}F_{10}FeN_4O$: 775.0274, found: 775.0282.

2.2.3. Synthesis of manganese (III) corroles

*10-(2-hydroxylphenyl)-5,15-bis(pentafluorophenyl)corrole manganese (III) (**Mn-2a**)*. A solution of 10-(2-*h*ydroxylphenyl)-5,15-bis(pentafluorophenyl)corrole (21.9 mg, 0.03 mmol) and manganese acetate

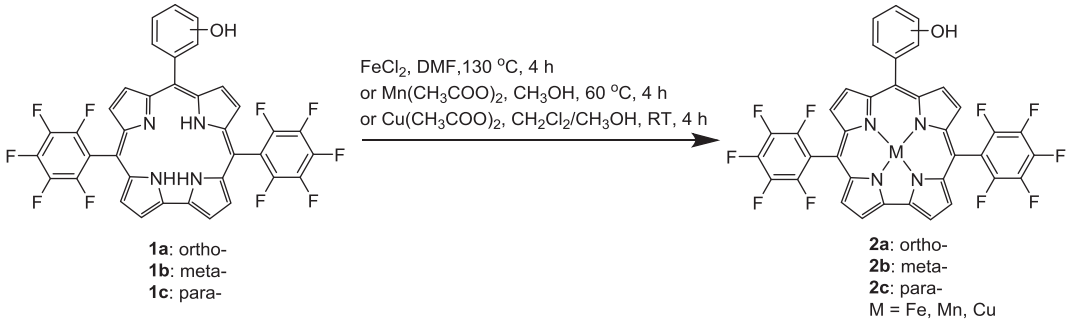

Scheme 1. Synthesis of metallocorroles.

tetrahydrate (406.0 mg, 1.66 mmol) in CH_3OH (10 mL) was refluxed for 4 h. The reaction mixture was allowed to cool down to room temperature, then CH_2Cl_2 (30 mL) and H_2O (30 mL) were added to the reaction mixture, followed by stirring vigorously for 5 min. The organic phase was collected and washed six times with deionized water, dried over Na_2SO_4, filtered and evaporated under reduced pressure to afford crude product. The resulting crude product was purified by chromatography on silica gel with CH_2Cl_2/CH_3OH (100:2) as eluent. The pure product was obtained after recrystallization from CH_2Cl_2/hexane. Yield: 73.74%. HRMS-ESI: *m/z*: calcd. for $C_{37}H_{12}F_{10}MnN_4O$: 774.0305, found: 774.0313.

10-(3-hydroxylphenyl)-5,15-bis(pentafluorophenyl)corrole manganese (III) ***(Mn-2b)***. The synthetic method was similar with **Mn-2a**. Yield: 86.35%. HRMS-ESI: *m/z*: calcd. for $C_{37}H_{12}F_{10}MnN_4O$: 774.0305, found: 775.0297.

10-(4-hydroxylphenyl)-5,15-bis(pentafluorophenyl)corrole manganese (III) ***(Mn-2c)***. The synthetic method was similar to **Mn-2a**. Yield: 55.14%. HRMS-ESI: *m/z*: calcd. for $C_{37}H_{12}F_{10}MnN_4O$: 774.0305, found: 774.0319.

2.2.4. Synthesis of copper (III) corroles

10-(2-hydroxylphenyl)-5,15-bis(pentafluorophenyl)corrole copper (III) ***(Cu-2a)***. A solution of 10-(2-*h*ydroxylphenyl)-5,15-bis(pentafluorophenyl)corrole (29.3 mg, 0.04 mmol) and copper acetate tetrahydrate (680.6 mg, 2.78 mmol) in CH_3OH/CH_2Cl_2 (1:1, 14 mL) were stirred for 4 h at room temperature. The reaction mixture was extracted with CH_2Cl_2, the organic phases were washed with water six times, then evaporated under reduced pressure to afford crude product. The resulting crude product was purified by chromatography on silica gel with CH_2Cl_2 as eluent. The pure product was obtained after recrystallization from CH_2Cl_2/hexane. Yield: 79.57%. HRMS-ESI: *m/z*: calcd. for $C_{37}H_{12}F_{10}CuN_4O$: 805.0118 $[M+Na]^+$, found:805.0115 $[M+Na]^+$.

10-(3-hydroxylphenyl)-5,15-bis(pentafluorophenyl)corrole copper (III) ***(Cu-2b)***. The synthetic method was similar to **Cu-2a**. Yield: 88.12%. HRMS-ESI: *m/z*: calcd. for $C_{37}H_{12}F_{10}CuN_4O$: 782.0220, found: 782.0216.

10-(4-hydroxylphenyl)-5,15-bis(pentafluorophenyl)corrole copper (III) ***(Cu-2c)***. The synthetic method was similar to **Cu-2a**. Yield: 89.87%. HRMS-ESI: *m/z*: calcd. for $C_{37}H_{12}F_{10}CuN_4O$: 782.0220, found: 782.0218.

2.3. DNA binding experiment

2.3.1. UV–vis spectrum titration experiments

Biological-grade calf thymus DNA (CT-DNA) was obtained from Sigma-Aldrich (US). All DNA binding experiments involving CT-DNA stock solution were performed in 5 mM Tris-HCl buffer solution (5 mM Tris, 50 mM NaCl, pH 7.2). A solution of CT-DNA in the Tris-HCl buffer gave a ratio of UV absorbance at 260 and 280 nm of ca. 1.8–1.9, indicating that the DNA was sufficiently free of the protein [29]. The concentration of CT-DNA was determined on the basis of the concentration of the nucleotide and was calculated using an extinction coefficient of 6600 $M^{-1}\cdot cm^{-1}$ at 260 nm. The absorbance titration experiments were carried out with a metallocorroles concentration of 10 μM in 5% DMF. All of the samples were initially pre-equilibrated with CT-DNA for 5 min before recording each spectrum. The intrinsic binding constant K_b of metallocorroles with CT-DNA could be determined from the increase in absorbance at Soret band and calculated using the following equation with absorption spectral titration data [30]:

$$[DNA]/(\varepsilon_a - \varepsilon_f) = [DNA]/(\varepsilon_b - \varepsilon_f) + 1/[K_b((\varepsilon_b - \varepsilon_f))] \quad (1)$$

where ε_a is the apparent extinction coefficient of the complex in the presence of CT-DNA, and ε_f and ε_b are the extinction coefficient of the complex when free and fully bound to CT-DNA, respectively. [DNA] is the concentration of CT-DNA in the base pairs. From the fit plots of $[DNA]/(\varepsilon_a - \varepsilon_f)$ versus [DNA], K_b was obtained by the ratio of the slope to the intercept.

2.3.2. Competitive DNA binding studies

Emission spectra were recorded by increasing the concentration of the metallocorroles in 3 mL of a solution of ethidium bromide (EB) plus CT-DNA in 5 mM Tris-HCl buffer solution with the excitation wavelength set at 370 nm. The changes in emission spectra were recorded after each successive addition of 3 μL metallocorroles (2 mM) and incubated for 5 min in the range of 500–700 nm. The quenching constants *K*sv and quenching rate constants *K*q calculated using the classical Stern-Volmer equation [31]:

$$F_0/F = 1 + K_{SV}[Q] = 1 + K_q\tau[Q] \quad (2)$$

where F and F_0 are emission intensities in the presence and absence of metallocorroles. K_{SV} and τ are a linear Stern-Volmer quenching constant and average lifetime of biomolecular with quencher (10^{-8} s). [*Q*] is the concentration of the quenchers.

2.4. In vitro experiment

2.4.1. Cytotoxicity assays

3-(4,5-Dimethylthiazole)-2,5-diphenyltetraazolium bromide (MTT) assay procedures were used to examine the *in-vitro* cytotoxicity of metallocorroles. Cells were placed in 96-well culture plates (5×10^3 cells per well) and grown overnight at 37 °C in a 5% CO_2 incubator. Metallocorroles were dissolved in DMSO and diluted with culture medium (final DMSO concentration, 1% *V/V*), then added to the monolayer (final concentration of corrole ranging from 1×10^{-6} to 1×10^{-4} mol/L). Control wells were prepared under the same conditions without complex. After incubation at 37 °C in a 5% CO_2 for 4 h, the plates were taken out from the incubator and the cells were irradiated by LED (625 ± 2 nm, 0.3 W/cm^2) at 20 cm distance for 1 h and then further incubated for 42 h. The stock MTT dye solution (20 μL, 5 mg/mL) was added to each well. After 4 h, DMSO (100 μL) was added to solubilize the MTT formazan. The optical density of each well was measured with a microplate spectrophotometer at a wavelength of 490 nm. Each experiment was repeated at least three times to obtain the mean values. The cell controls with 1% DMSO is shown in Fig. S18, 1% DMSO had no significant effect on cell survival without metallocorroles.

2.4.2. Nuclear staining

A549 cells were firstly seeded (2×10^5 cells per well) in 12 well plates, then treated with **Fe-2c** (60 μM) and illuminated by LED (625 ± 2 nm, 0.3 W/cm^2) at 20 cm distance for 1 h and then further incubated for 24 h. Untreated cells were used as the control group. Cell apoptosis was evaluated by using Hoechst-33258 (5 μg/mL) as described previously, and visualized by using a fluorescence microscope.

2.4.3. Cell cycle studies

A549 cells (1×10^6) were treated with **Fe-2c** (20 and 60 μM), and illuminated by LED (625 ± 2 nm, 0.3 W/cm^2) at 20 cm distance for 1 h. After 24 h, cells were treated with pancreatin to get from the plate, and rinsed with PBS twice. After centrifuging, cells were fixed with 75% ethanol overnight. Then, the fixed cells were centrifuged to remove the ethanol. After rinsing with PBS, cells were incubated with 20 mL of RNase A (0.2 mg/mL) and 20 mL of propidium iodide (0.02 mg/mL) for 30 min in the dark. The cells without **Fe-2c** and light were used as a negative control. After incubating with PI and filtering, cells were analyzed using a flow cytometer. The percentage of cycle distribution cells was also determined.

2.4.4. Reactive oxygen species (ROS) level detection

A549 cells were seeded into 12-well plates at a density of 2×10^5 cells per well and incubated for 24 h at 37 °C in 5% CO_2. The medium

was removed and replaced with medium containing **Fe-2c** (20 and 50 μM). The medium was removed and replaced with medium containing **Fe-2c** (20 and 50 μM). After incubation at 37 °C in 5% CO_2 for 4 h, the cells were illuminated by LED (625 ± 2 nm, 0.3 W/cm^2) at 20 cm distance for 1 h. Followed by incubation for 18 h, the medium was removed. The fluorescent dye 2′,7′-dichlorodihydrofluorescein diacetate (DCHF-DA, 10 mM) was added to the medium and the cells were imaged by fluorescence microscopy.

2.4.5. Mitochondrial membrane potential assay

A549 cells in a growth medium (2×10^5 cells/well) were seeded on a sterilized coverslip in 12-well plates and grown overnight at 37 °C in a 5% CO_2 incubator. **Fe-2c** was added to the wells and incubated at 37 °C in 5% CO_2 for 4 h, then cells were exposed to the red light (625 ± 2 nm, 0.3 W/cm^2) at 20 cm distance for 1 h. After incubation for 18 h, the cells were incubated for 20 min with 1 mg/mL of 5,5′,6,6′-tetrachloro-1,1′,3,3′-tetraethyl-imidacarbocyanine iodide (JC-1) in culture medium at 37 °C in the dark. The cell pellets were suspended in PBS and then imaged under a fluorescence microscope.

2.4.6. Apoptosis assay by flow cytometry

A549 cells were layered on six-well plates at a density of 1×10^6 cells per well for 24 h. The medium was removed and replaced with **Fe-2c**. The cells were incubated for 4 h, then irradiated by LED (625 ± 2 nm, 0.3 W/cm^2) at 20 cm distance for 1 h and continuously incubated for other 18 h. 1×10^6 cells were harvested, washed with PBS, and then stained with a fluorescent probe containing 50 mg/mL PI and 1 mg/mL Annexin V-FITC in PBS in the dark for 15 min. Cells were analyzed using a flow cytometer.

3. Results and discussion

3.1. Chemistry

3.1.1. Synthesis and characterization

Corroles **1a-c** were prepared by using previously published method [19]. They were all fully characterized by ^{1}H, ^{19}F NMR spectroscopy. The ^{1}H NMR spectral data of corroles **1a-c** showed expected profiles of *trans*-A_2B-corroles. For example, corrole **1a**, the doublets at δ 9.13 and 9.12, 8.73 and 8.72, 8.69 and 8.68, 8.59 and 8.57 ppm were assigned to the resonances of β-pyrrolic protons. The resonances signs of the protons of the phenyl rings appeared at chemical shift δ 7.92, 7.70 and 7.34 ppm. In the ^{19}F NMR spectrum of corrole **1a**, the phenyl *meta*-fluorine resonance appeared a multiplet signal at δ −161.41 ppm. The resonances of *para*-fluorine atoms appeared a triplet peak at δ −152.49 ppm, and *ortho*-fluorine atoms appeared a multiplet at around δ −137.60 ppm. The corresponding metallocorroles were synthesized by reaction of freebase corroles and the metal salt in different organic solvents (DMF, MeOH, DCM). The final metallocorrole products were obtained by column purification and characterized by UV–vis and HRMS-ESI spectra. All original NMR and HRMS-ESI spectra were listed in supplementary information (Figs. S1–S15).

3.1.2. Electronic absorption spectra

Fig. 1 shows UV–Vis spectra of prepared metallocorroles in DMF and DMSO. All metallocorroles exhibited typical corrole absorption, an intense Soret band at around 400 nm, corresponds to π–π* electronic transition from ground state (S0) to the second excited state (S2), and three less intense Q bands at 500–600 nm, originated from π–π* electronic transitions from ground state (S0) to the first excited state (S1) [32]. Interestingly, all manganese(III) corroles display a distinctive split-Soret band at about 400–425 nm, a broad Q-band around 600 nm, and a solvent sensitive absorption at about 480–490 nm which is assigned as the metal-ligand charge transfer band [15]. While iron(III) and copper(III) corroles didn't exhibit solvent sensitive absorption except for **Cu-2c** in DMF (Fig. S16). The photophysical parameters of all metallocorroles in both DMF and DMSO solvents are summarized in Table 1.

3.2. DNA binding studies

3.2.1. UV–Vis spectrum titrations

The binding mode between small molecules and DNA may be monitored by UV–Vis titration method [33]. As is well known, the magnitudes of spectral change are dependent on the binding modes between porphyrinoids and DNA. The intercalative binding usually results in a large bathochromic shift ($\Delta\lambda \geq 15$ nm), and strong hypochromism ($H \geq 35\%$) at Soret band due to the more intimate contact with the π system. For external binding, the absorption spectra maximum exhibits a small bathochromic shift ($\Delta\lambda \leq 8$ nm) and weak hypochromism ($H \leq 10\%$) [34]. Fig. S17 shows the absorption spectra changes of metallocorroles at a constant concentration with increasing concentrations of CT-DNA. The weak hypochromism and negligible bathochromic shift in the Soret bands of all of metallocorroles suggests that these corroles bind to CT-DNA through external binding mode [28,35,36]. The binding constants of metallocorroles with CT-DNA were range from 0.68×10^5 to 2.94×10^5 M^{-1}, which is comparable to the reported manganese(III) or iron(III) porphyrins [36]. Moreover, compared to corresponding *meta*- and *para*-hydroxyl metallocorroles, all *ortho*-hydroxyl metallocorroles exhibited a less binding affinity. The binding constant and spectra changing parameters are listed in Table 2.

3.2.2. Competitive binding experiments

It has been observed that DNA, manganese(III) corroles, iron(III) corroles and copper(III) corroles exhibit negligibly fluorescence in the buffer solution. Therefore, a competitive binding experiment was used to further investigate the DNA binding of these metallocorroles, in which ethidium bromide (EB) was used as a fluorescence probe. The quenching constants (*K*sv) and quenching rate constants (*K*q) were calculated by Eq. (2). The fluorescence spectra of EB bound to DNA in the absence and presence of metallocorroles are shown in Fig. 2. The emission intensity of EB decreases obviously with increasing the concentration of metallocorroles. Considering EB is a strong intercalator and the outside binding mode between DNA and these metallocorroles, the observed fluorescence quenching maybe caused by a static quenching process via the formation of metallocorroles-EB-DNA conjugates [35,37,38]. The measured quenching constants are comparable to binding constants obtained from UV–Vis titration. The *meta*- and *para*- hydroxyl metallocorroles exhibited larger quenching constants than their *ortho*-hydroxyl counterparts.

3.3. In vitro photodynamic activities

3.3.1. Cytotoxicity

The cytotoxicity of metallocorroles were determined using MTT assay with doses ranging from 1.56 μmol to 100 μmol under dark or light irradiation. Four carcinoma A549 (lung), HepG2 (liver), MCF-7 (breast), DU145 (prostate) and one normal cell line GES-1 (gastric epithelial) had been tested. The mitochondrial enzyme succinate dehydrogenase in living cells will cause the cleavage of MTT tetrazolium salt into formazan which is a blue colored compound [39], this can be used to determine the cell viability. The resulting IC_{50} values of metallocorroles to different cell lines are listed in Table 3. All metallocorroles were basically noncytotoxic toward normal cells GES-1 whether under light or dark conditions when their concentrations were less than 100 μmol. But they showed significant dark or photo-cytotoxicity to tumor cells and which was dependent on the tumor cell types. Iron (III) corroles exhibited higher dark cytotoxicity and photocytotoxicity to A549, HepG2 and MCF-7 than manganese(III) and copper(III) corroles. Except metallocorrole **Cu-2c**, all other metallocorroles were noncytotoxic to DU145 cells with or without illumination. **Fe-2c** didn't show the obvious dark cytotoxicity to A549 cell lines when its

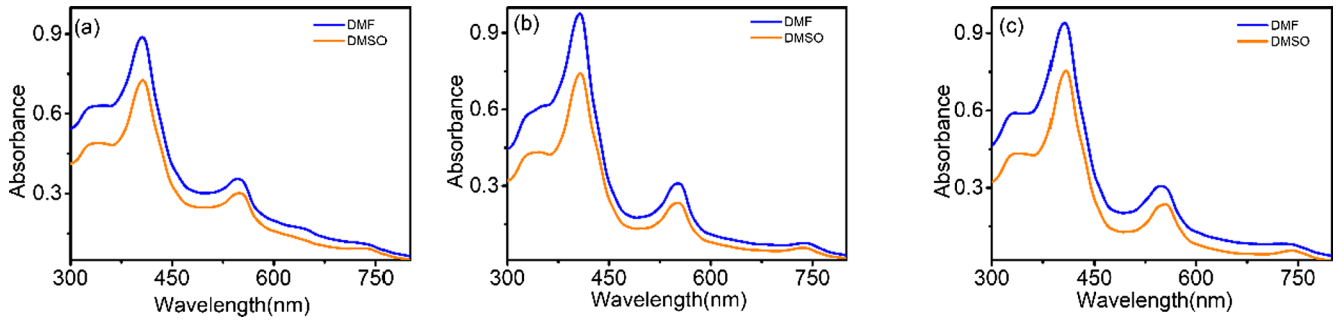

Fig. 1. Normalized UV–vis absorption spectra of metallocorroles **Fe-2a** (a), **Fe-2b** (b) and **Fe-2c** (c) in DMF or DMSO.

Table 1
Electronic absorption data for various metallocorroles.

Corrole	Absorption [nm] (Lgε/cm^{-1} M^{-1})				
	Soret band			Q-band	
Fe-2a	406(4.65)			546(4.25)	
	407(4.56)			549(4.18)	
Fe-2b	407(4.69)			552(4.19)	
	408(4.57)			552(4.07)	
Fe-2c	406(4.67)			547(4.18)	
	408(4.58)			554(4.07)	
Mn-2a	396(4.57)	417(4.59)	481(4.59)	581(4.13)	628(4.16)
	396(4.61)	418(4.63)	481(4.57)	579(4.21)	631(4.23)
Mn-2b	398(4.58)	419(4.60)	482(4.48)	581(4.10)	632(4.13)
	397(4.61)	424(4.64)	481(4.58)	579(4.14)	633(4.18)
Mn-2c	398(4.42)	422(4.60)	483(4.48)	581(4.10)	635(4.12)
	397(4.60)	429(4.64)	483(4.58)	579(4.23)	638(4.17)
Cu-2a	432(4.74)			600(4.14)	
	432(4.72)			610(4.22)	
Cu-2b	421(4.74)			575(3.68)	602(3.86)
	405(4.73)			550(3.77)	579(3.73)
Cu-2c	400(4.75)	430(4.68)		553(3.90)	579(3.89)
	405(4.73)			550(3.77)	579(3.73)

Table 2
Intrinsic binding constants of metallocorrole with CT-DNA.

Metallocorroles	$\Delta\lambda$[a]	H[b] (%)	K_b ($\times 10^5$ M^{-1})	K_{sv} ($\times 10^4$ M^{-1})	K_q ($\times 10^{12}$ M^{-1})
Fe-2a	0	4.84	0.68	3.05	3.05
Fe-2b	−1	4.89	2.38	8.48	8.48
Fe-2c	0	9.56	1.28	7.70	7.70
Mn-2a	1	5.08	0.74	6.31	6.31
Mn-2b	1	11.09	1.75	6.69	6.69
Mn-2c	0	11.45	2.94	6.81	6.81
Cu-2a	1	9.03	1.20	4.38	4.38
Cu-2b	0	10.01	2.24	4.04	4.04
Cu-2c	−1	12.52	2.20	7.77	7.77

[a] $\Delta\lambda$ represents the difference in Soret band of metallocorrole between free and bound CT-DNA states.

[b] H represents the hypochromism at Soret band, as defined by $H\% = (A_{free} - A_{bound})/A_{free} \times 100\%$ (A represents the absorbance).

concentration was less than 100 μM. However, it exhibited significant photocytotoxicity with a IC_{50} value of 30 ± 9 μM. The observed photocytotoxicity of **Fe-2c** is one-third of the cytotoxicity of *cis*-platin. This indicates **Fe-2c** is the best PDT photosensitizer against A549 cells. Based on this observation, **Fe-2c** and A549 cell lines was chosen for the flowing rest study.

3.3.2. Nuclear staining

Apoptosis is one of the major way for cell death. The classic characteristics of cell apoptosis are chromatin condensation, nuclear pyknosis and fragmented nuclei. The morphological changes of A549 cell nuclei were checked by staining with Hoechst 33258, a blue fluorescent DNA dye (Fig. 3). The control cells or **Fe-2c** treated cells under dark conditions presented normal euchromatin with deep blue color (Fig. 3A, C, E). This indicates that the tumor cell is resistant to metallocorrole **Fe-2c** treatment without irradiation. While after treatment with metallocorrole **Fe-2c** combined with light illumination, large tight blue spots and fragmental blue spots could be observed (Fig. 3G), suggesting the chromatin condensation and nuclei fragmentation of A549 cells. From bright field macroscopic image (Fig. 3H), the reduction of cell density and cell shrinkage could be observed. These observations suggested that **Fe-2c** PDT treatment could induce A549 cell apoptosis.

3.3.3. Cell cycle analysis

The cell cycle is a series of events leading to cell division and replication. The effect of **Fe-2c** PDT treatment on the cell cycle distribution of A549 cell lines were evaluated by flow cytometry using propidium iodide (PI) as chromatin staining dye (Fig. 4). Significant alternations in the cell phases of A549 cells could be observed after being treated with **Fe-2c** under illumination. As delineated in the cell cycle histogram of A549 cell lines in Fig. 4, the percentage of cells at sub-G1 phases was increased dose-dependently from 5.17% control to 8.16% and 10.2% when **Fe-2c** concentration increased from 20 μmol to 60 μmol. Accompanied by a decrease in G0/G1 and S phases, While G2/M phases percentage increased from 25.9% control to 33.0% and 45.5% respectively. The cell cycle distribution exhibited negligible change after 60 μmol **Fe-2c** treatment under dark conditions. The accumulation of cells in sub-G1 phase may be caused by degradation or fragmentation of DNA [40,41], which is related to cell apoptosis. In addition, the cell cycle was arrested at G2/M, implying the activation of G2/M checkpoint which is related to DNA lesions and will prevents or delays mitosis [42]. This observation is consistent with the PDT treatment of iridium(III) porphyrin to human non-small lung cancer cell line NCI-H460 [43] or 4,4′,4″-{20-[4-(Methoxycarbonyl)phenyl]-porphyrin-5,10,15-triyl}-tris(1-methylpyridin-1-ium) to PANC-1 cells [44]. Thus, cell cycle assay also demonstrated that **Fe-2c** was an apoptosis inducer under irradiation condition.

3.3.4. Measurement of intracellular ROS

Fe-2c induced reactive oxygen species (ROS) generation was detected by using 2′, 7 – dichlorofluorescin diacetate (DCFH-DA) as fluorescence probe and Rosup as positive control [45]. The non-fluorescent DCFH-DA can freely diffuse through the cell membrane, and hydrolyzed by intracellular esterase to form non-fluorescent DCFH which can't escape from the cell. The non-fluorescent DCFH will be rapidly oxidized to green fluorescent DCF by intracellular ROS. As shown in Fig. 5, no fluorescence could be observed in A549 cells incubated with PBS. When A549 cells were treated by **Fe-2c** combined with irradiation, a significant green fluorescence of DCF appeared, which was similar to Rosup. Under dark conditions, no fluorescence could be observed. These results indicated that **Fe-2c** PDT treatment can effectively induce ROS generation in A549 cells.

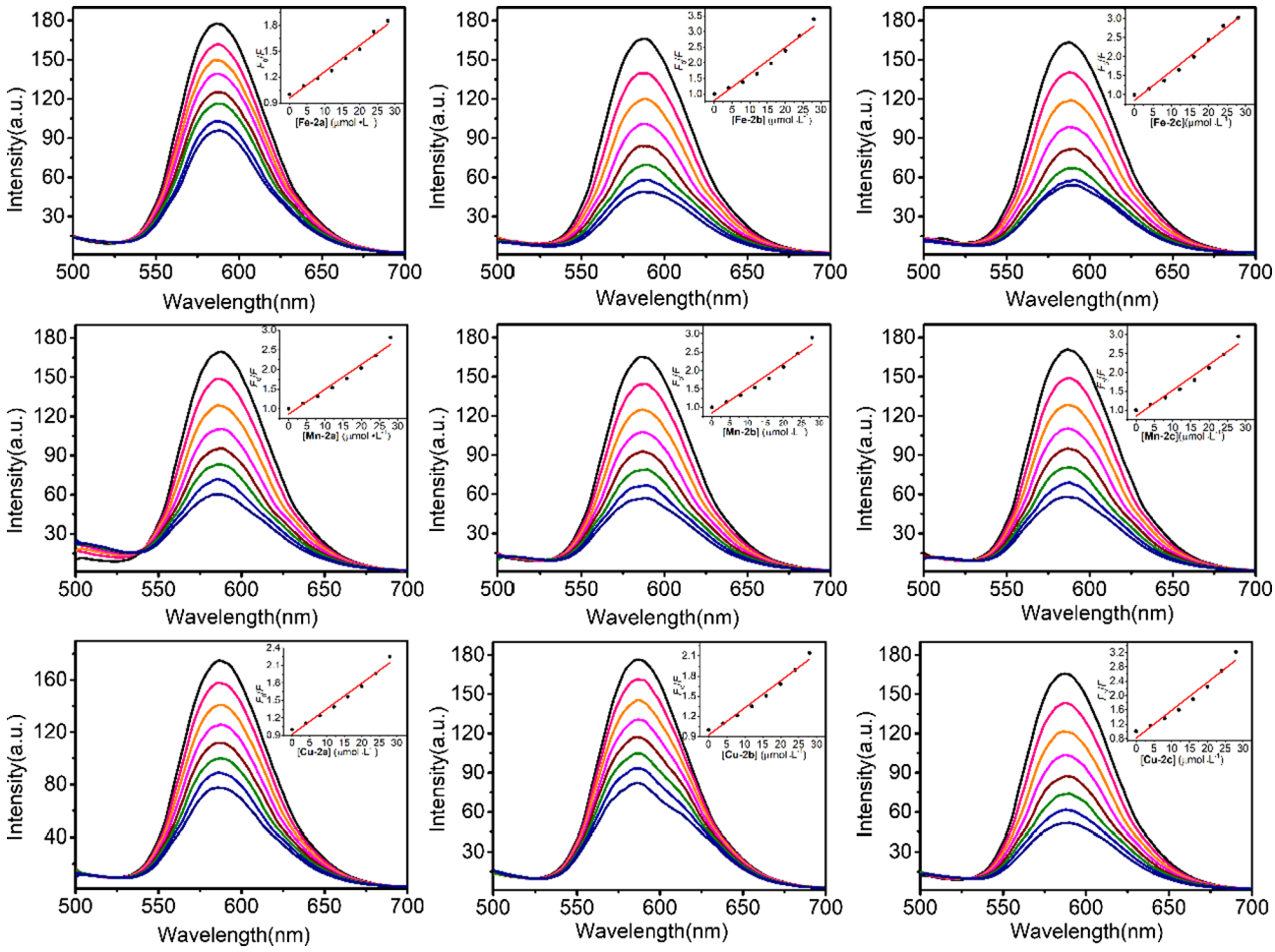

Fig. 2. Emission spectra of EB (5 μM) bound to CT-DNA (30 μM) by **Fe-2a** (a), **Fe-2b** (b), **Fe-2c** (c), **Mn-2a** (d), **Mn-2b** (e), **Mn-2c** (f), **Cu-2a** (g), **Cu-2b** (h), and **Cu-2c** (i). [corrole] = 0–28 μM.

3.3.5. Mitochondrial membrane potential assay

Mitochondria plays a crucial role in the apoptotic process. The dissipation of mitochondrial membrane potential ($\Delta\psi_m$) may be an early event in the apoptotic process [46]. Mitochondrial membrane potential (MMP) fluorescence probe (JC-1) was often used to monitor MMP. When mitochondrial membrane potential is normal, the JC-1 may accumulate in the matrix of mitochondria and form J-aggregates with red fluorescence. When mitochondrial membrane potential decreases, JC-1 is in its monomer form which emits green fluorescence.

The control cells showed red fluorescence due to the well-defined integral mitochondrial membrane with normal cristae structure (Fig. 6). When the A549 cell lines were treated with **Fe-2c** under illumination, strong green fluorescence could be observed due to the loss of $\Delta\psi_m$, which was similar CCCP positive control test. Under dark conditions, the A549 cells emitted strong red fluorescence, suggesting no loss of $\Delta\psi_m$. These results demonstrated that **Fe-2c** PDT treatment would result in the loss of the mitochondrial membrane potential. This may trigger the A549 cell apoptosis.

3.3.6. Cell apoptosis

The apoptosis assay of A549 cell lines was performed by propidium iodide (PI) and Annexin V-FITC double-labeled method using flow cytometry. The Annexin V-FITC is used to label extracellularly extruded phosphatidylserine translocation from the inner layer of the plasma

Table 3
The photocytotoxicity of metallocorroletowards different cell lines (IC_{50}/μM).

IC_{50}	A549		HepG2		MCF-7		DU145		GES-1	
	Dark	Light	Dark	Light	Dark	Light	Dark	Light	Dark	Light
Fe-2a	42 ± 14	24 ± 8	57 ± 18	43 ± 15	30 ± 4	20 ± 2	> 100	> 100	97 ± 3	97 ± 6
Fe-2b	22 ± 4	18 ± 3	27 ± 7	15 ± 2	74 ± 25	27 ± 4	> 100	> 100	> 100	> 100
Fe-2c	> 100	30 ± 9	> 100	> 100	> 100	> 100	> 100	> 100	> 100	> 100
Mn-2a	> 100	> 100	> 100	> 100	> 100	> 100	> 100	> 100	> 100	> 100
Mn-2b	49 ± 24	38 ± 20	> 100	> 100	> 100	> 100	> 100	> 100	> 100	> 100
Mn-2c	45 ± 17	23 ± 8	56 ± 21	25 ± 6	> 100	> 100	> 100	> 100	> 100	> 100
Cu-2a	77 ± 40	85 ± 6	9 ± 1	5 ± 1	> 100	> 100	> 100	> 100	> 100	> 100
Cu-2b	> 100	> 100	> 100	54 ± 12	> 100	> 100	85 ± 8	9 ± 4.	> 100	> 100
Cu-2c	> 100	> 100	> 100	> 100	> 100	> 100	> 100	> 100	> 100	> 100
Cis-platin	8 ± 1		10 ± 1		30 ± 4		7 ± 1		9 ± 1	

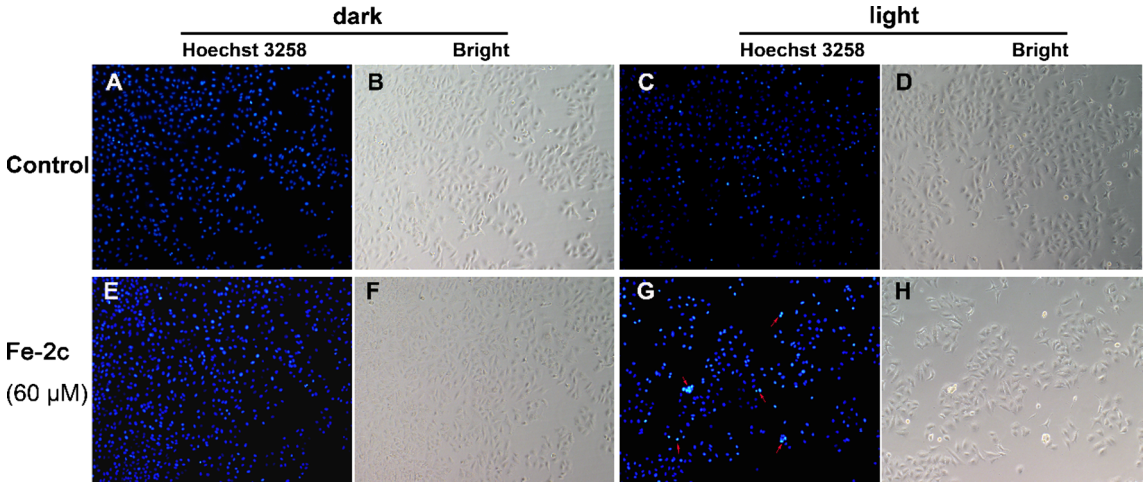

Fig. 3. Fluorescence microscopic images of Hoechst 33258-stained A549 cells with **Fe-2c** PDT treatment.

membrane, which occurs during early apoptotic processes. While PI is used to stain the nuclear components of cells that have lost the plasma membrane integrity in necrotic or late-stage apoptotic processes. Upon illumination, A549 cell lines treated with **Fe-2c** displayed a concentration-dependently decrease in the percentage of the live cells (Annexin V-FITC-/PI-), which decreased from 96.5% control to 72.1% (20 μmol) and 47.9% (40 μmol) respectively (Fig. 7). At the same time, the percentage of cells at early apoptotic stage (Annexin V-FITC+/PI−) increased significantly from 1.24% control to 10.8% 40 μmol **Fe-2c**. The necrotic or late-stage apoptotic cells (Annexin V-FITC+/PI+) induced by **Fe-2c** of 20 μmol and 40 μmol was 25.2% and 39.7% respectively, which were remarkably higher than control 2.13%. Under dark conditions, **Fe-2c** had no effect on A549 cell lines.

4. Conclusions

In summary, the tested metallocorroles exhibited variable cytostatic activity and cytotoxicity against some of the human cancer cell lines, while they are non-toxic for human normal cell lines. Spectroscopic evidences suggest that these metallocorroles interact with CT-DNA via

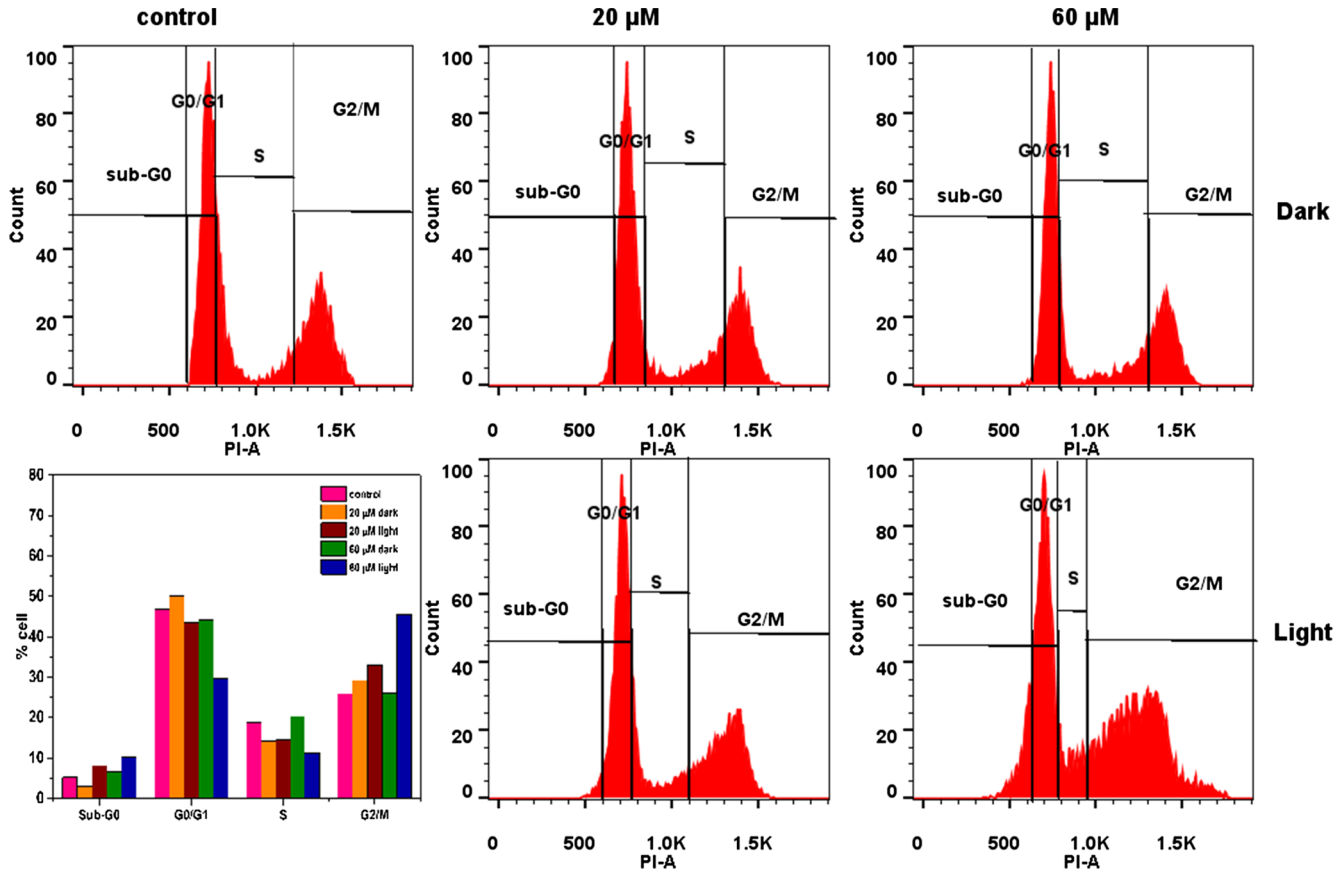

Fig. 4. Flow cytometry of A549 cells after PDT treatment with **Fe-2c** at different concentrations (PI staining).

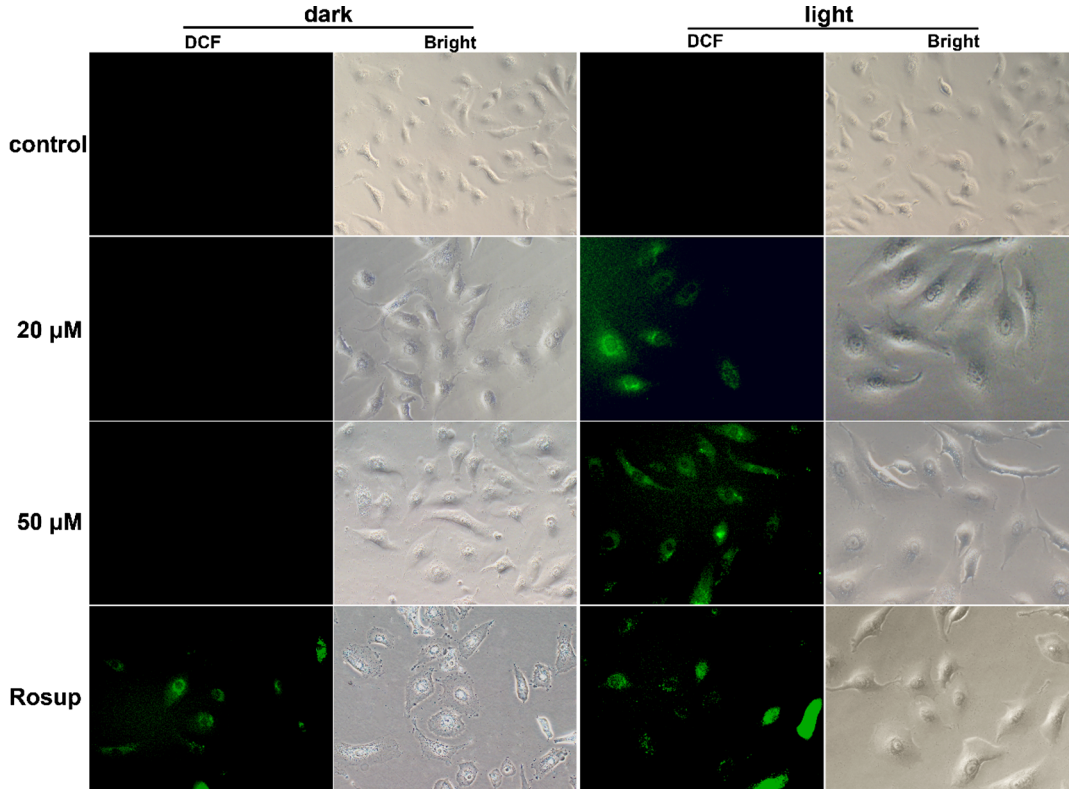

Fig. 5. Intracellular ROS detection in A549 after PDT treatment with **Fe-2c**.

outside binding mode. Metallocorrole **Fe-2c** has significant photodynamic activity and low dark toxicity to A549 cells. The PDT treatment of A549 cell lines by metallocorrole **Fe-2c** will cause the cell arrest at the G2/M stage, enhancement of the cellular ROS level and destruction of the mitochondrial membrane potential, which will finally induce cell apoptosis and necrosis. The present work demonstrates iron (III) corrole has the potential application in anticancer photodynamic therapy.

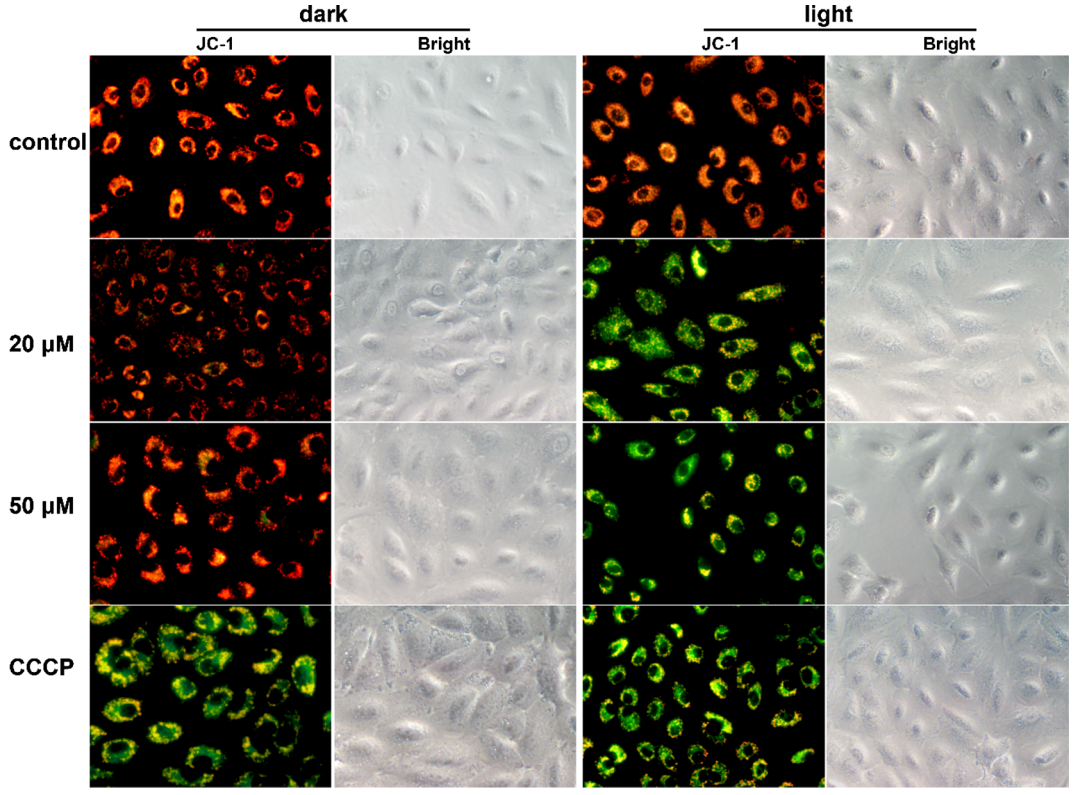

Fig. 6. Effect of **Fe-2c** PDT treatment on the MMP in A549 cells.

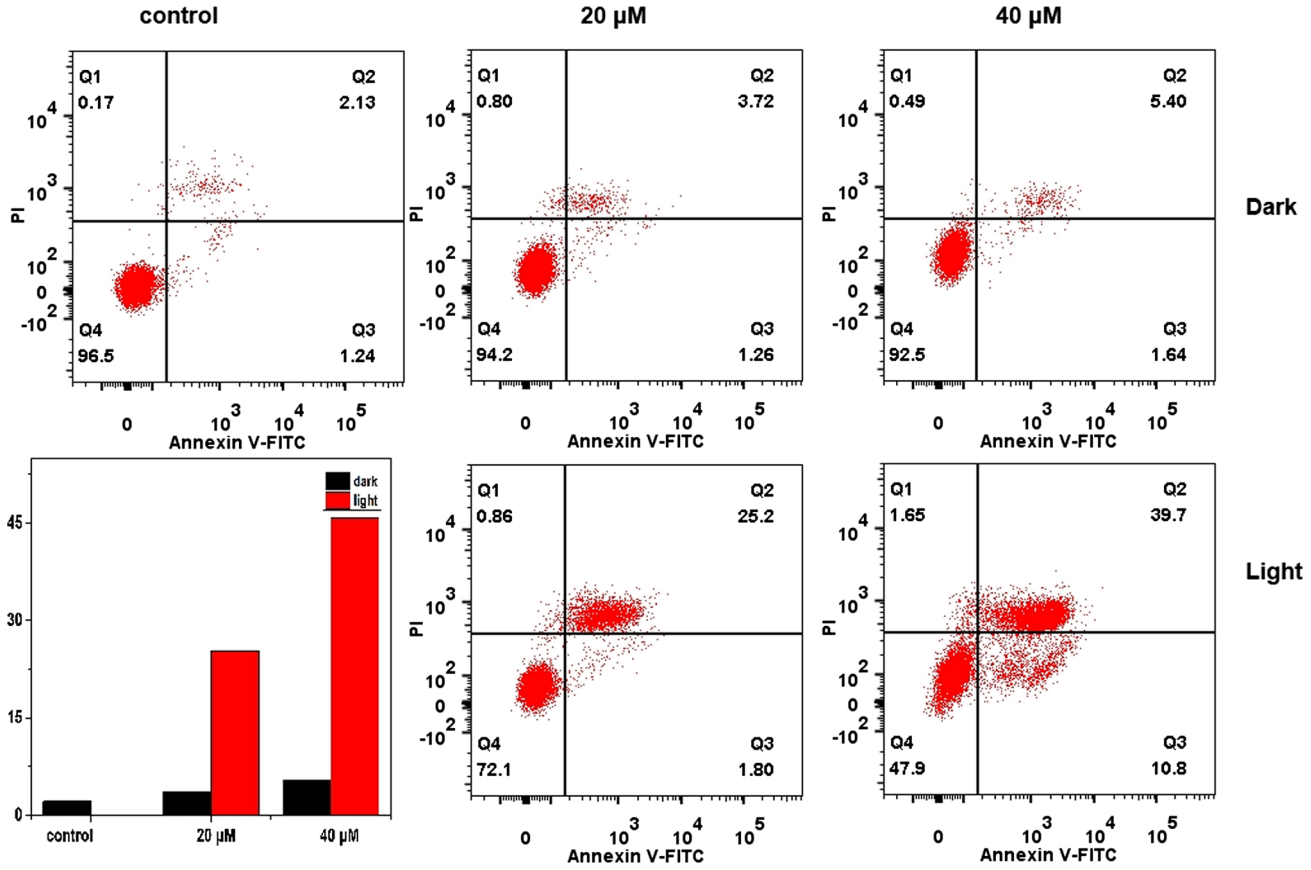

Fig. 7. Flow cytometry of A549 cells detected with Annexin-V/PI double staining after PDT treatment with **Fe-2c.**

Acknowledgements

We gratefully acknowledge financial support from the National Natural Science Foundation of China (No. 21671068).

Appendix A. Supplementary material

Supplementary data to this article can be found online at https://doi.org/10.1016/j.bioorg.2019.103085.

References

[1] S. Monro, K.L. Colón, H. Yin, J. Roque, P. Konda, S. Gujar, R.P. Thummel, L. Lilge, C.G. Cameron, S.A. McFarland, Transition metal complexes and photodynamic therapy from a tumor-centered approach: challenges, opportunities, and highlights from the development of tld1433, Chem. Rev. (2018), https://doi.org/10.1021/acs.chemrev.8b00211.

[2] S.B. Brown, E.A. Brown, I. Walker, The present and future role of photodynamic therapy in cancer treatment, Lancet. Oncol. 5 (2004) 497–508, https://doi.org/10.1016/S1470-2045(04)01529-3.

[3] D.E.J.G.J. Dolmans, D. Fukumura, R.K. Jain, Photodynamic therapy for cancer, Nat. Rev. Cancer 3 (2003) 380, https://doi.org/10.1038/nrc1071.

[4] A.P. Castano, P. Mroz, M.R. Hamblin, Photodynamic therapy and anti-tumour immunity, Nat. Rev. Cancer. 6 (2006) 535, https://doi.org/10.1038/nrc1894.

[5] T.K. Horne, M.J. Cronjé, Mechanistics and photo-energetics of macrocycles and photodynamic therapy: an overview of aspects to consider for research, Chem. Biol. Drug Des. 89 (2017) 221–242, https://doi.org/10.1111/cbdd.12761.

[6] P. Agostinis, K. Berg, K.A. Cengel, T.H. Foster, A.W. Girotti, S.O. Gollnick, S.M. Hahn, M.R. Hamblin, A. Juzeniene, D. Kessel, M. Korbelik, J. Moan, P. Mroz, D. Nowis, J. Piette, B.C. Wilson, J. Golab, Photodynamic therapy of cancer: an update, CA Cancer J. Clin. 61 (2011) 250–281, https://doi.org/10.3322/caac.20114.

[7] A. Gomes, M. Neves, J.A.S. Cavaleiro, Cancer, photodynamic therapy and porphyrin-type derivatives, An. Acad. Bras. Cienc. 90 (2018) 993–1026, https://doi.org/10.1590/0001-3765201820170811.

[8] J.P. Celli, B.Q. Spring, I. Rizvi, C.L. Evans, K.S. Samkoe, S. Verma, B.W. Pogue, T. Hasan, Imaging and photodynamic therapy: mechanisms, monitoring, and optimization, Chem. Rev. 110 (2010) 2795–2838, https://doi.org/10.1021/cr900300p.

[9] N.L. Oleinick, H.H. Evans, The photobiology of photodynamic therapy: cellular targets and mechanisms, Radiat. Res. 150 (1998) S146–S156, https://doi.org/10.1073/pnas.0901531106.

[10] R.D. Teo, J.Y. Hwang, J. Termini, Z. Gross, H.B. Gray, Fighting cancer with corroles, Chem. Rev. 117 (2017) 2711–2729, https://doi.org/10.1021/acs.chemrev.6b00400.

[11] A. Mahammed, Z. Gross, Corroles as triplet photosensitizers, Coord. Chem. Rev. (2017), https://doi.org/10.1016/j.ccr.2017.08.028.

[12] I. Aviv, Z. Gross, Corrole-based applications, Chem. Commun. (2007) 1987–1999, https://doi.org/10.1039/B618482K.

[13] C.I.M. Santos, Corroles: synthesis, functionalization and application as chemosensors, ChemistryOpen 3 (2014) 88–92, https://doi.org/10.1002/open.201402001.

[14] A. Haber, M. Aviram, Z. Gross, Variables that influence cellular uptake and cytotoxic/cytoprotective effects of macrocyclic iron complexes, Inorg. Chem. 51 (2012) 28–30, https://doi.org/10.1021/ic202204u.

[15] H.-Y. Liu, M.H.R. Mahmood, S.-X. Qiu, C.K. Chang, Recent developments in manganese corrole chemistry, Coord. Chem. Rev. 257 (2013) 1306–1333, https://doi.org/10.1016/j.ccr.2012.12.017.

[16] P. Lim, A. Mahammed, Z. Okun, I. Saltsman, Z. Gross, H.B. Gray, J. Termini, Differential cytostatic and cytotoxic action of metallocorroles against human cancer cells: potential platforms for anticancer drug development, Chem. Res. Toxicol. 25 (2012) 400–409, https://doi.org/10.1021/tx200452w.

[17] R.A. Baglia, J.P.T. Zaragoza, D.P. Goldberg, Biomimetic reactivity of oxygen-derived manganese and iron porphyrinoid complexes, Chem. Rev. 117 (2017) 13320–13352, https://doi.org/10.1021/acs.chemrev.7b00180.

[18] D. Aviezer, S. Cotton, M. David, A. Segev, N. Khaselev, N. Galili, Z. Gross, A. Yayon, Porphyrin analogues as novel antagonists of fibroblast growth factor and vascular endothelial growth factor receptor binding that inhibit endothelial cell proliferation, tumor progression, and metastasis, Cancer Res. 60 (2000) 2973–2980 http://cancerres.aacrjournals.org/content/60/11/2973.long.

[19] C.K. Chang, P.W. Kong, H.Y. Liu, L.L. Yeung, H.K. Koon, N.K. Mak, Synthesis and photodynamic activities of modified corrole derivatives on nasopharyngeal carcinoma cells, SPIE BiOS, 2006; SPIE: 2006; p. 11. https://doi.org/10.1117/12.646328.

[20] H. Agadjanian, J. Ma, A. Rentsendorj, V. Valluripalli, J.Y. Hwang, A. Mahammed, D.L. Farkas, H.B. Gray, Z. Gross, L.K. Medina-Kauwe, Tumor detection and elimination by a targeted gallium corrole, Proc. Natl. Sci. USA 106 (2009) 6105–6110, https://doi.org/10.1073/pnas.0901531106.

[21] M. Pribisko, J. Palmer, R.H. Grubbs, H.B. Gray, J. Termini, P. Lim, Cellular uptake and anticancer activity of carboxylated gallium corroles, Proc. Natl. Sci. USA 113 (2016) E2258–E2266, https://doi.org/10.1073/pnas.1517402113.

[22] F. Cheng, L. Huang, H. Wang, Y. Liu, J. Kandhadi, H. Wang, L. Ji, H. Liu, Photodynamic therapy activities of 10-(4-formylphenyl)-5, 15-bis (pentafluorophenyl) corrole and its gallium complex, Chin. J. Chem. 35 (2017) 86–92, https://doi.org/10.1002/cjoc.201600633.
[23] Z. Zhang, H.H. Wang, H.J. Yu, Y.Z. Xiong, H.T. Zhang, L.N. Ji, H.Y. Liu, Synthesis, characterization and in vitro and in vivo photodynamic activity of gallium (iii) tris (ethoxycarbonyl) corrole, Dalton T. (2017), https://doi.org/10.1039/c7dt00992e.
[24] Z. Zhang, H.-J. Yu, H. Huang, H.-H. Wang, S. Wu, H.-Y. Liu, H.-T. Zhang, The photodynamic activity and toxicity evaluation of 5,10,15-tris(ethoxylcarbonyl) corrole phosphorus(v) in vivo and in vitro, Eu. J. Med. Chem. 163 (2019) 779–786, https://doi.org/10.1016/j.ejmech.2018.12.031.
[25] R. Socoteanu, G. Manda, R. Boscencu, G. Vasiliu, A. Oliveira, Synthesis, spectral analysis and preliminary in vitro evaluation of some tetrapyrrolic complexes with 3d metal ions, Molecules 20 (2015) 15488, https://doi.org/10.3390/molecules200915488.
[26] G. Lan, K. Ni, Z. Xu, S.S. Veroneau, Y. Song, W. Lin, Nanoscale metal–organic framework overcomes hypoxia for photodynamic therapy primed cancer immunotherapy, J. Am. Chem. Soc. 140 (2018) 5670–5673, https://doi.org/10.1021/jacs.8b01072.
[27] G. Zuber, J.C. Quada, S.M. Hecht, Sequence selective cleavage of a DNA octanucleotide by chlorinated bithiazoles and bleomycins, J. Am. Chem. Soc. 120 (1998) 9368–9369, https://doi.org/10.1021/ja981937r.
[28] A. D'Urso, S. Nardis, G. Pomarico, M.E. Fragalà, R. Paolesse, R. Purrello, Interaction of tricationic corroles with single/double helix of homopolymeric nucleic acids and DNA, J. Am. Chem. Soc. 135 (2013) 8632–8638, https://doi.org/10.1021/ja4023539.
[29] J. Marmur, A procedure for the isolation of deoxyribonucleic acid from micro-organisms, 208-IN1, J. Mol. Biol. 3 (1961), https://doi.org/10.1016/S0022-2836(61)80047-8.
[30] M. Sari, J. Battioni, D. Dupre, D. Mansuy, J.B. Le Pecq, Interaction of cationic porphyrins with DNA: Importance of the number and position of the charges and minimum structural requirements for intercalation, Biochemistry 29 (1990) 4205–4215, https://doi.org/10.1021/bi00469a025.
[31] J.-T. Huang, X.L. Wang, Y. Zhang, M.H. Mahmood, Y.Y. Huang, X. Ying, L.N. Ji, H.Y. Liu, DNA binding and nuclease activity of a water-soluble sulfonated manganese(iii) corrole, Transit. Met. Chem. 38 (2013) 283–289, https://doi.org/10.1007/s11243-013-9689-5.
[32] L. Giribabu, K. Jain, K. Sudhakar, N. Duvva, R. Chitta, Light induced intramolecular electron and energy transfer events in rigidly linked borondipyrromethene: Corrole dyad, J. Lumin. 177 (2016) 209–218, https://doi.org/10.1016/j.jlumin.2016.03.038.
[33] R. Palchaudhuri, P.J. Hergenrother, DNA as a target for anticancer compounds: methods to determine the mode of binding and the mechanism of action, Curr. Opin. Biotechnol. 18 (2007) 497–503, https://doi.org/10.1016/j.copbio.2007.09.006.
[34] D.R. McMillin, A.H. Shelton, S.A. Bejune, P.E. Fanwick, R.K. Wall, Understanding binding interactions of cationic porphyrins with b-form DNA, Coord. Chem. Rev. 249 (2005) 1451–1459, https://doi.org/10.1016/j.ccr.2004.11.016.
[35] C. Hahn da Silveira, E.N. Garoforo, O.A. Chaves, P.F.B. Gonçalves, L. Streit, B.A. Iglesias, Synthesis, spectroscopy, electrochemistry and DNA interactive studies of meso-tetra(1-naphthyl)porphyrin and its metal complexes, Inorg. Chim. Acta 482 (2018) 542–553, https://doi.org/10.1016/j.ica.2018.06.052.
[36] L. Shi, Y.-Y. Jiang, T. Jiang, W. Yin, J.-P. Yang, M.-L. Cao, Y.-Q. Fang, H.-Y. Liu, Water-soluble manganese and iron mesotetrakis(carboxyl)porphyrin: DNA binding, oxidative cleavage, and cytotoxic activities, Molecules 22 (2017), https://doi.org/10.3390/molecules22071084.
[37] B.C. Baguley, M. Le Bret, Quenching of DNA-ethidium fluorescence by amsacrine and other antitumor agents: a possible electron-transfer effect, Biochemistry 23 (1984) 937–943, https://doi.org/10.1021/bi00300a022.
[38] J. Olmsted III, D.R. Kearns, Mechanism of ethidium bromide fluorescence enhancement on binding to nucleic acids, Biochemistry 16 (1977) 3647–3654, https://doi.org/10.1021/bi00635a022.
[39] T.F. Slater, B. Sawyer, U. Sträuli, Studies on succinate-tetrazolium reductase systems: Iii. Points of coupling of four different tetrazolium salts iii. Points of coupling of four different tetrazolium salts, Biochim. Biophys. Acta 77 (1963) 383–393, https://doi.org/10.1016/0006-3002(63)90513-4.
[40] Z. Zhang, J.-Y. Wen, B.-B. Lv, X. Li, X. Ying, Y.-J. Wang, H.-T. Zhang, H. Wang, H.-Y. Liu, C.K. Chang, Photocytotoxicity and g-quadruplex DNA interaction of water-soluble gallium(iii) tris(n-methyl-4-pyridyl)corrole complex, Appl. Organomet. Chem. 30 (2016) 132–139, https://doi.org/10.1002/aoc.3408.
[41] D. Simoni, F.P. Invidiata, R. Rondanin, S. Grimaudo, G. Cannizzo, E. Barbusca, F. Porretto, N. D'Alessandro, M. Tolomeo, Structure − activity relationship studies of novel heteroretinoids: Induction of apoptosis in the hl-60 cell line by a novel isoxazole-containing heteroretinoid, J. Med. Chem. 42 (1999) 4961–4969, https://doi.org/10.1021/jm991059n.
[42] G. Lossaint, E. Besnard, D. Fisher, J. Piette, V. Dulić, Chk1 is dispensable for g2 arrest in response to sustained DNA damage when the atm/p53/p21 pathway is functional, Oncogene 30 (2011) 4261, https://doi.org/10.1038/onc.2011.135.
[43] T.-L. Lam, K.-C. Tong, C. Yang, W.-L. Kwong, X. Guan, M.-D. Li, V. Kar-Yan Lo, S. Lai-Fung Chan, D. Lee Phillips, C.-N. Lok, C.-M. Che, Luminescent ruffled iridium (iii) porphyrin complexes containing n-heterocyclic carbene ligands: structures, spectroscopies and potent antitumor activities under dark and light irradiation conditions, Chem. Sci. (2018), https://doi.org/10.1039/C8SC02920B.
[44] U. Chilakamarthi, D. Koteshwar, S. Jinka, N. Vamsi Krishna, K. Sridharan, N. Nagesh, L. Giribabu, Novel amphiphilic g-quadruplex binding synthetic derivative of tmpyp4 and its effect on cancer cell proliferation and apoptosis induction, Biochemistry (2018), https://doi.org/10.1021/acs.biochem.8b00843.
[45] L. Bourré, S. Thibaut, A. Briffaud, N. Rousset, S. Eléouet, Y. Lajat, T. Patrice, Indirect detection of photosensitizer ex vivo, J. Photochem. Photobiol. B: Biol. 67 (2002) 23–31, https://doi.org/10.1016/S1011-1344(02)00279-8.
[46] J.D. Ly, D.R. Grubb, A. Lawen, The mitochondrial membrane potential (δψm) in apoptosis; an update, Apoptosis 8 (2003) 115–128, https://doi.org/10.1023/A:1022945107762.